ADVANCED ELECTRONIC MATERIALS
www.advelectronicmat.de

Very High Density (>10^{14} cm^{-2}) Polarization-Induced 2D Hole Gases Observed in Undoped Pseudomorphic InGaN/AlN Heterostructures

Reet Chaudhuri, Zexuan Zhang, Huili Grace Xing, and Debdeep Jena*

High hole densities are desired in p-channel field effect transistors to improve the speed and on-currents. Building on the recently discovered undoped, polarization-induced GaN/AlN 2D hole gas (2DHG), this work demonstrates the tuning of the piezoelectric polarization difference across the heterointerface by introducing indium in the GaN channel. Using careful design and epitaxial growths, these pseudomorphic (In)GaN/AlN heterostructures result in some of the highest carrier densities of >10^{14} cm^{-2} in a III-nitride heterostructure—just an order below the intrinsic crystal limit of ≈10^{15} cm^{-2}. These ultra-high density InGaN/AlN 2DHGs show room temperature mobilities of 0.5–4 cm^2 V^{-1} s^{-1} and do not freeze out at low temperatures. A characteristic alloy fluctuation energy of 1.0 eV for hole scattering in InGaN alloy is proposed based on the experiments.

1. Introduction

The presence of intrinsic polarization [1] in III-nitride semiconductors have been used to generate high mobility 2D electron gases (2DEGs) by utilizing the positive polarization discontinuity across a heterointerface since the early 1990s. These have yielded as-grown 2DEG densities [2,3] ranging from low-5 × 10^{12} to high 5 × 10^{13} cm^{-2} without the need of donor dopants. These 2DEGs have a high room temperature mobility of 1400–1800 cm^2 V^{-1} s^{-1} resulting in low sheet resistances <200 Ω per sq. The recently discovered [4,5] high-density 2D hole gas (2DHG) in undoped GaN/AlN heterostructures have proved that the same principle of polarization generates 2D confined holes at a negative polarization difference interface without acceptor doping. Compared to the inefficient p-type acceptor doping using magnesium (Mg), [6] these polarization-induced 2DHGs enable some of the highest conductivity single-channel p-type layers in GaN. The densities of 5 × 10^{13} cm^{-2} in these structures represent some of the highest 2D hole gas densities among III-nitride semiconductor heterostructures as they utilize the full intrinsic polarization discontinuity between the GaN and AlN, as opposed to previously reported (Al,In)GaN/GaN or InGaN/GaN interfaces.[7–10] 2D carrier densities higher than 1 × 10^{14} cm^{-2} have not been measured in III-nitride semiconductor heterostructures so far, neither in an as-grown structure nor field-effect induced channel, for electrons or holes.

Even though these GaN 2DHGs typically have resistances which are orders of magnitude higher than those of 2DEGs, these are critical to realize GaN p-channel field effect transistors (FETs). These p-channel FETs combined with GaN n-channel high electron mobility transistors (HEMTs) will enable complementary GaN circuits [11] for energy efficient electronics in the future.

Recently, the aforementioned GaN/AlN high-density 2DHGs were used as the channel to break the GHz-speed barrier for the first time in GaN p-channel FETs [12] with record high on-currents greater than 0.4 A mm^{-1} and f_t/f_{max} of 23/40 GHz. In these devices, the as-grown 2DHG density is partially depleted under the gate using a recess etch. However the access resistances are determined by the as-grown 2DHG conductivity and therefore the density. If the 2DHG density is engineered to be higher in the access regions, the resultant lower access resistance should further enhance the on-currents, transconductance and therefore operation speeds of these state-of-art GaN p-channel FETs.

In this work very high 2DHG densities >1 × 10^{14} cm^{-2} are demonstrated in carefully designed and grown pseudomorphic InGaN layers on thick, relaxed AlN buffer layers. It is shown that introduction of indium in the strained GaN channel of a GaN/AlN structure boosts the resulting mobile charge densities, primarily because of the increase in piezoelectric component of polarization in the strained InGaN layer. This work represents the first report of polarization-induced carrier densities greater than 1 × 10^{14} cm^{-2} at a single III-nitride heterointerface, which is just an order below the atomic limit of 10^{15} cm^{-2}. The best hole mobilities in these high-density 2DHGs are found to be ≈5 cm^2 V^{-1} s^{-1} at 300 K and ≈15 cm^2 V^{-1} s^{-1} at 10 K. These are

R. Chaudhuri, Z. Zhang, H. G. Xing, D. Jena
School of Electrical and Computer Engineering
Cornell University
Ithaca, NY 14583, USA
E-mail: rtc77@cornell.edu
H. G. Xing, D. Jena
Department of Material Science and Engineering
Cornell University
Ithaca, NY 14583, USA
H. G. Xing, D. Jena
Kavli Institute Nanoscience
Cornell University
Ithaca, NY 14583, USA

The ORCID identification number(s) for the author(s) of this article can be found under https://doi.org/10.1002/aelm.202101120.

DOI: 10.1002/aelm.202101120

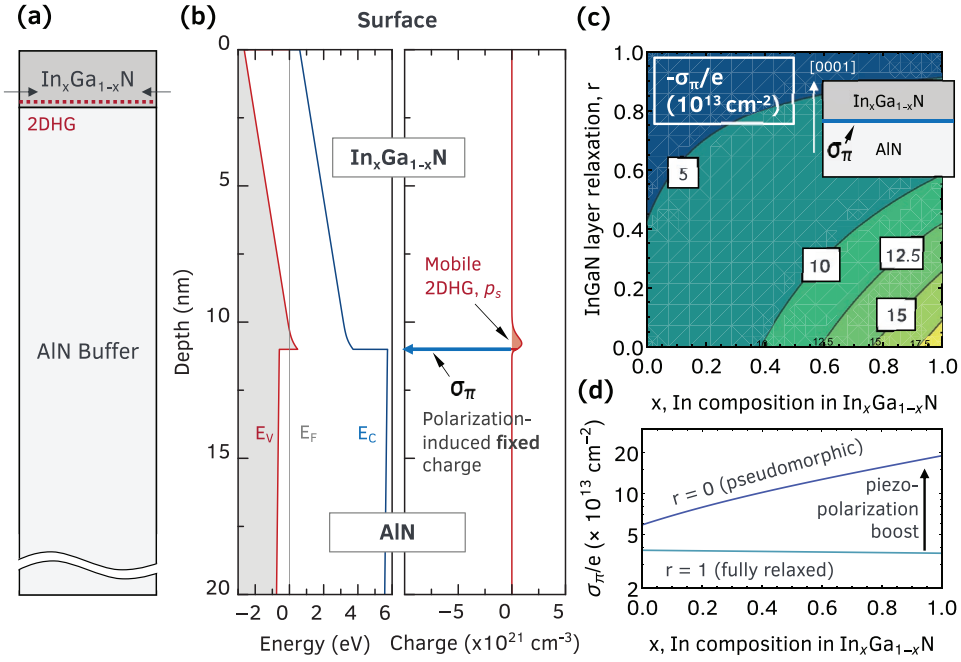

Figure 1. a) Metal-polar undoped InGaN/AlN heterostructure with the expected 2DHG at the interface studied in this work. b) A simulated band diagram and charge profile for 11 nm $In_{0.07}Ga_{0.93}N$ on AlN buffer layer, showing the negative polarization-induced fixed sheet charge σ_π at the InGaN/AlN interface which is partly compensated by the mobile 2DHG of density p_s. c) Contour plot of the expected σ_π in this hetereostructure as a function of the InGaN layer relaxation r and In composition x in the InGaN layer. d) The 1D profiles along the $r = 0$ and $r = 1$ is plotted. An increase in polarization fixed charge is expected on increasing In composition while maintaining pseudomorphic compressive strain in the layer.

lower than ≈25 $cm^2\ V^{-1}\ s^{-1}$ and ≈200 $cm^2\ V^{-1}\ s^{-1}$ at 300 and 10 K respectively seen in GaN/AlN 2DHGs. These lower mobilities are shown to be due to the dominance of alloy disorder scattering at room temperatures. By comparing the experimental data to a simple scattering model, the InGaN/AlN 2DHG system allows the direct measurement of the alloy fluctuation potential of 1.0 eV for holes in InGaN.

2. Heterostructure Design

When a metal-polar GaN or InGaN crystal is epitaxially grown on a thick AlN buffer layer, as shown in **Figure 1**a, a fixed negative sheet charge σ_π arises due to the intrinsic polarization field discontinuity (ΔP) at the InGaN/AlN interface. The polarization in III-nitride semiconductors has two components—the spontaneous polarization P_{SP} and the piezoelectric polarization P_{PZ}. Assuming a linear interpolation between the physical properties[13] of InN and GaN, the polarization-induced fixed sheet charge σ_π is given by[1]

$$\begin{aligned}\sigma_\pi(x,r) &= P_{SP}^{InGaN} - P_{SP}^{AlN} - P_{PZ}^{InGaN} \\ &= P_{SP}^{InGaN} - P_{SP}^{AlN} - 2\varepsilon_{xx}\left(e_{31} - e_{33}\frac{C_{13}}{C_{33}}\right) \\ &= \Delta P_{SP} - 2\frac{a(r)-a_0}{a_0}\left(e_{31} - e_{33}\frac{C_{13}}{C_{33}}\right)\end{aligned} \quad (1)$$

where $e_{31/33}$ are the piezoelectric coefficients and $C_{13/33}$ are the elastic constants of InGaN. ε_{xx} is the isotropic in-plane strain in the InGaN layer, given by $\epsilon_{xx} = (a(r) - a_0)/a_0$ where a_0 is the relaxed in-plane lattice constant of InGaN, and $a(r)$ is the lattice constant of the strained InGaN film on AlN. a_0, $e_{31/33}$, $C_{13/33}$ are functions of the indium composition x and are assumed to be linear interpolation of corresponding values for GaN ($x = 0$) and InN ($x = 1$).

An InGaN layer grown on AlN is ideally expected to be compressively strained throughout the composition range as both GaN (a_0^{GaN} = 3.189 Å) and InN (a_0^{InN} = 3.553 Å) have larger in-plane lattice constant than AlN (a_0^{AlN} = 3.112 Å). However, a real crystal tends to relax to release the built-up strain energy. The actual epitaxial strain relationship between InGaN crystal and AlN buffer layer underneath is represented by the relaxation r through the relation $a = r\cdot(a_0 - a_0^{AlN}) + a_0^{AlN}$. $r = 0$ represents a pseudomorphic InGaN layer on AlN whereas $r = 1$ represents a fully relaxed InGaN layer on AlN. Therefore the σ_π is a function of the InGaN composition x and film relaxation r.

The simulated charge and energy band profile for a metal-polar 11 nm InGaN layer on AlN with x = 0.07 is shown in Figure 1b. The polarization-induced negative fixed charge σ_π at the InGaN/AlN interface is indicated in the charge profile. If the InGaN layer is sufficiently thick,[4] then σ_π is partly compensated by mobile holes which are confined by the valence band offset at the InGaN/AlN interface to form a mobile 2D hole gas (2DHG). Within this model, the σ_π therefore represents the maximum achievable 2DHG density p_s in a given InGaN/AlN structure.

The upper limit of sheet density σ_π in metal-polar InGaN/AlN heterostructures is calculated as a function of x and r using Equation 1 and the known values of elastic and polarization

constants.[1,13] The results are shown as a contour plot in Figure 1c. The profiles along $r = 0$ and $r = 1$ are plotted in Figure 1d. At $x = 0$ and $r = 0$, that is, in a pseudomorphic GaN/AlN structure, $\sigma_\pi \approx 5 \times 10^{13}$ cm^{-2}. This agrees with the experimentally measured 2DHG densities in undoped GaN/AlN interfaces.[4] In a fully relaxed InGaN film ($r = 1$), σ_π decreases with increasing In composition x. This is because InN has a lower spontaneous polarization P_{SP} than GaN. However, the lattice mismatch between InGaN and AlN increases with x, increasing the strain ϵ_{xx} and thereby increasing the P_{PZ} contribution to the σ_π. The net effect is a boost in σ_π from $\approx 5 \times 10^{13}$ cm^{-2} for GaN/AlN to $>1.5 \times 10^{14}$ cm^{-2} for InN/AlN. Therefore, a pseudomorphically strained InGaN layer on AlN should result in a higher σ_π and consequently higher 2DHG concentrations than those in GaN/AlN structures.

The epitaxial growth of pseudomorphic InGaN layers on AlN is particularly challenging due to different thermal stability and lattice mismatch. InN starts decomposing at ≈630 °C, which is below the optimal molecular beam epitaxy (MBE) growth temperature[17,18] of AlN of ≈750–1000 °C. This necessitates a growth interruption to lower the temperature before InGaN deposition. Additionally, due to the lattice mismatch with respect to the AlN substrate, there exists a finite InGaN coherent critical thickness h_c beyond which it relieves the strain energy by forming misfit dislocations[16,19] and no longer remains pseudomorphic to AlN. Using the Fischer model[16] of strain relaxation, the critical thickness h_c of InGaN grown on (relaxed) AlN and GaN substrates are calculated as a function of the In composition x. The calculated values are plotted as solid lines in **Figure 2**a,b. Previous experimental reports of pseudomorphic InGaN grown on GaN[14,15] agree well with the calculation in Figure 2a, validating the model. For InGaN on AlN heterostructures, the expected h_c decreases with increasing In composition x—from 15 nm for $x = 0$, to 3 nm for $x = 1$, as shown in Figure 2b. The h_c of 15 nm for GaN/AlN ($x = 0$) concurs with the previous experimental observation[4] of 13 nm pseudomorphic GaN on AlN. According to this model, low-composition $x < 0.1$ InGaN layers thinner than ≈15–10 nm should be pseudomorphically strained to the underlying AlN, with expected charge $\sigma_\pi > 5 \times 10^{13}$ cm^{-2}.

Additionally, for the fixed charges σ_π to be compensated by a mobile 2DHG, the InGaN layer needs to be thicker than a certain critical thickness d_0 beyond which the polarization dipole is neutralized by carriers from the surface states. For example, in an AlN/GaN 2DEG,[20] $d_0 \approx 1$ nm. For a GaN/AlN 2DHG, this critical thickness has been experimentally found[4] to be $d_0 \approx 3$ nm.

Thus, considering the above trade-offs, it is expected that ≈3–15 nm thick, low-composition $x < 0.1$ undoped InGaN layers grown on AlN should be pseudomorphically strained and yield mobile 2DHGs with densities higher than 5×10^{13} cm^{-2}.

3. Results and Discussion

To test this, a series of InGaN on AlN heterostructures were grown using plasma assisted MBE (PA-MBE). The details of the growth are provided in Experimental Section. The structures grown and their transport properties are summarized in **Table 1**.

Atomic force microscopy (AFM) scans of all samples except sample F showed smooth surface morphology with root mean square (rms) roughnesses of <1 nm. Sample F had a rougher surface with island-like features and a rms roughness of >1 nm. Scans from samples A and D are shown in **Figure 3**a. Atomic steps were visible forming spiral features, a characteristic of a screw dislocation mediated MBE-growth.[21] The other samples in Table 1 exhibited similar surface morphology. X-ray diffraction (XRD) scans along (002) symmetric peak for selected samples A, D, and G are shown in Figure 3b. The InGaN compositions and the layer thicknesses are estimated from

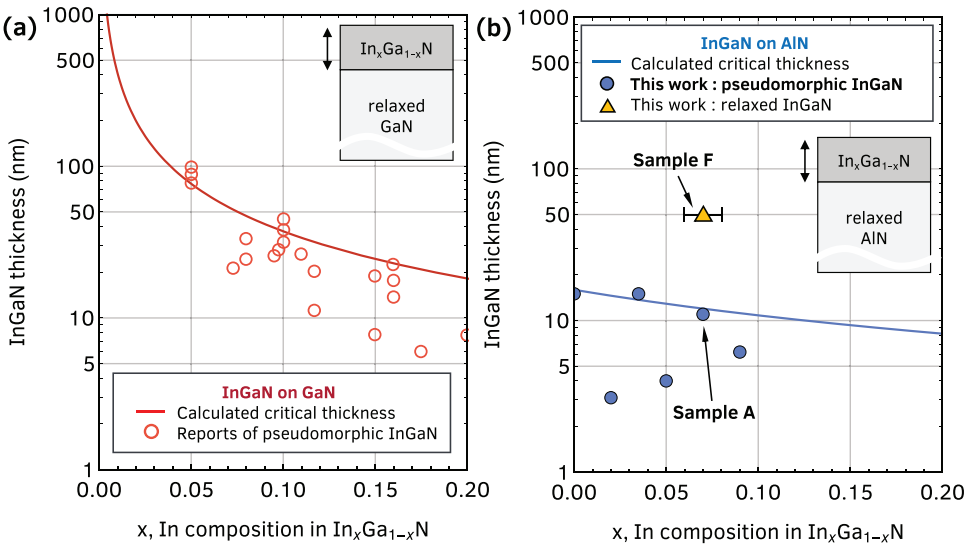

Figure 2. a) Previous experimental reports of pseudomorphic InGaN layers on GaN[14,15] compared with the calculated critical coherent thickness[16] of InGaN on GaN to validate the model. b) The predicted critical coherent thickness[16] of InGaN on AlN as a function of In composition. The experimental data points from InGaN on AlN samples grown using MBE in this work are also included. The pseudomorphically strained InGaN layers on AlN all lie below the critical thickness line, agreeing with the theoretical prediction. The X-ray diffraction reciprocal space maps of samples A and F are shown in Figure 3c,d.

Table 1. Structural details of the InGaN/AlN heterostructures studied in this work, with their corresponding 2DHG densities p_s, mobilities μ_p measured via Hall-effect at 300 and 77 K. Sheet resistance R_s of $>10^3$ $k\Omega$ per sq. indicates resistive samples in which the transport could not be extracted using Hall effect measurements. All samples had a ≈400 nm thick AlN buffer layer grown on metal-polar AlN on Sapphire template and were unintentionally-doped (UID). The mean values of the Hall-effect results are shown here across multiple measurements on co-loaded samples. All conductive samples exhibited positive Hall-coefficient confirming the presence of mobile holes.

ID	Channel layer	p_s^{300K} [10^{14} cm^{-2}]	μ_p^{300K} [cm^2 V^{-1} s^{-1}]	R_s^{300K} [$k\Omega$ per sq.]	p_s^{77K} [10^{14} cm^{-2}]	μ_p^{77K} [cm^2 V^{-1} s^{-1}]	R_s^{77K} [$k\Omega$ per sq.]
A	11 nm $In_{0.07}Ga_{0.93}N$	1.43	3.6	16.2	0.56	9.84	10.6
B	4 nm $In_{0.05}Ga_{0.95}N$	3.15	0.27	73.5	2.36	0.54	49
C	3.1 nm $In_{0.02}Ga_{0.98}N$	–	–	$>10^3$	–	–	$>10^3$
D	6.2 nm $In_{0.09}Ga_{0.91}N$	4.29	0.95	15.3	2.29	2.27	21.34
E	15 nm $In_{0.06}Ga_{0.94}N$	1.5	2.2	17.6	0.52	9.5	10.7
F	50 nm $In_{0.07}Ga_{0.93}N$	–	–	$>10^3$	–	–	$>10^3$
G	13 nm GaN	0.46	23.11	5.9	3.4	105	1.7

the (002) peak position and the fringe spacings respectively. The extracted data for all samples are summarized in Table 1. XRD reciprocal space mapping (RSM) around asymmetric AlN (105) peak was performed to characterize the strain in the InGaN layers and compare with the critical thickness predictions. Apart from sample F, the InGaN layers in the other samples were also confirmed to be fully strained to AlN. One of the scans from sample A with a 11 nm of $In_{0.07}Ga_{0.93}N$ layer is shown in Figure 3c. The relative positions of the InGaN and AlN (105) peaks clearly confirm that the InGaN layer is pseudomorphically strained to AlN. The experimental data for samples A–E, plotted in Figure 2b, lie below the predicted critical thickness of InGaN/AlN, agreeing with the calculations. To further validate this model, sample F with a thick ≈50 nm of $In_{0.07}Ga_{0.93}N$ layer on AlN was also grown under similar conditions and characterized. Since 50 nm is above the predicted critical thickness in Figure 2b, the film is expected to relax. The XRD RSM for sample F, shown in Figure 3d, confirms that it is indeed the case and that the 50 nm InGaN layer has partly relaxed and is no longer pseudomorphic strained to the AlN. A partial relaxation of ≈61% is extracted from the RSM. This gradual relaxation of the thick InGaN film also leads to a spread in In composition of 7 ± 1% in sample F, which is attributed to compositional pulling effects previously observed in AlGaN.[22] Such a spread of composition is not seen in the other pseudomorphically strained samples A–E. The strain relaxation also partly explains the rougher surface morphology observed in sample F. To the authors' best knowledge, this is the first controlled study of pseudomorphic epitaxial growth of InGaN layers directly on AlN.

Thus, the InGaN/AlN samples A-E have the desired structures in which a high-density 2DHG is expected. Hall-effect measurements were performed on the samples using soldered corner indium contacts confirm the presence of the 2DHG.

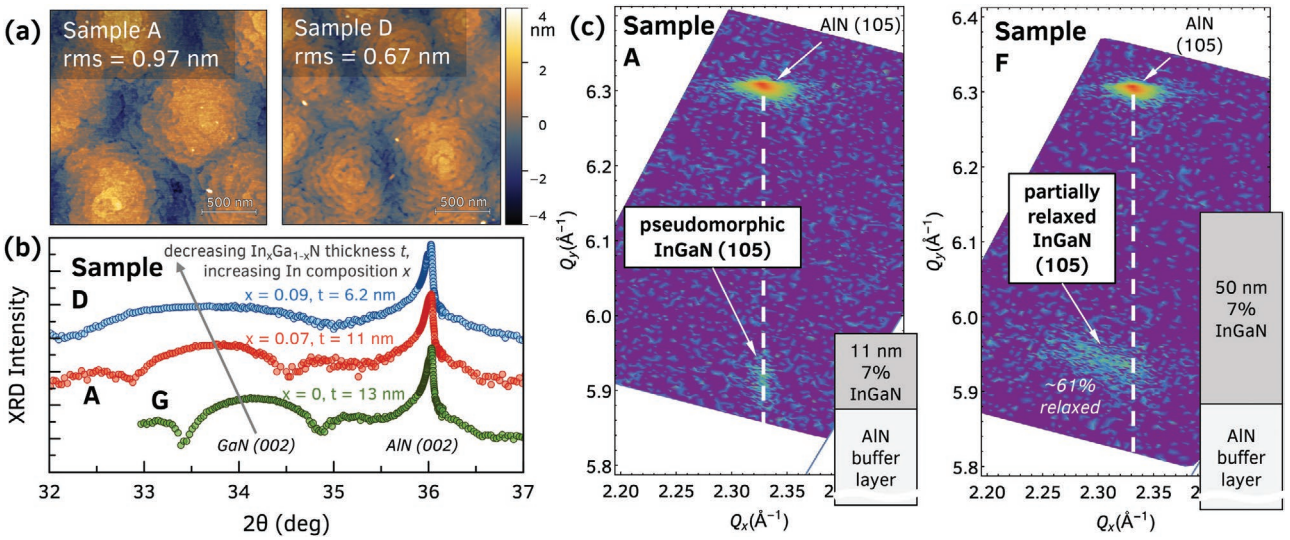

Figure 3. a) Representative AFMs of the surface of pseudomorphic InGaN/AlN heterstructures, samples A and D in Table 1. Atomic steps are visible forming spirals around threading dislocations with a screw component. b) An X-ray diffraction (XRD) symmetric coupled scan along (002) showing the position of the In peak change with the InGaN composition which allows estimation of the thickness and the composition of the layer. c) XRD reciprocal space map (RSM) of sample A and sample F around the AlN (105) asymmetric peak confirming an 11 nm $In_{0.07}Ga_{0.93}N$ layer is pseudomorphically-strained to the AlN buffer whereas a 50 nm thick $In_{0.07}Ga_{0.93}N$ layer on AlN is relaxed. This agrees well to the calculated curves in Figure 2b of critical thickness of InGaN/AlN.

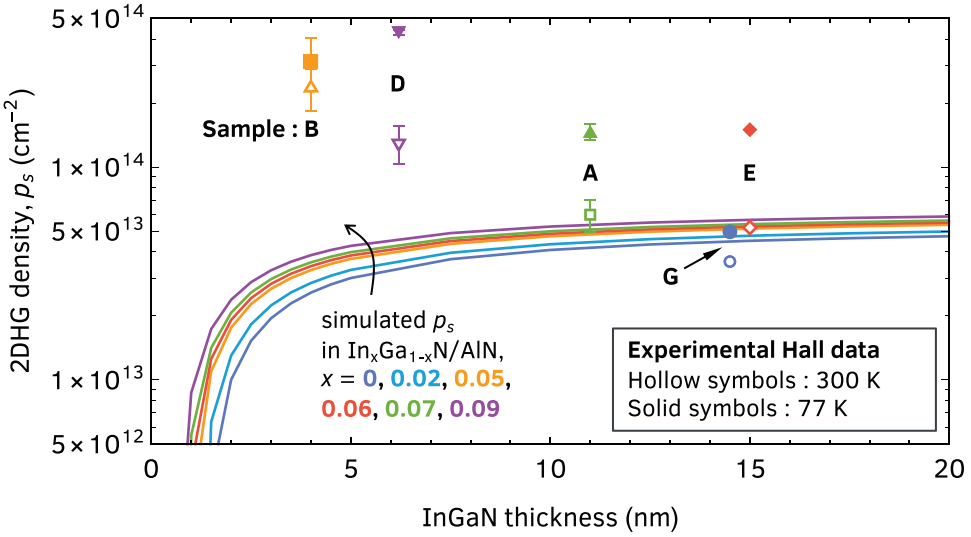

Figure 4. The 300 and 77 K Hall-effect measured 2DHG densities p_s in the InGaN/AlN heterostructures plotted as a function of InGaN layer thickness. The expected p_s at 300 K from a self-consistent 1D Schrodinger Poisson solver are also plotted for comparison. No significant change in p_s is expected upon cooling to 77 K from the simulations.

First, a control sample with just the AlN buffer layer without any InGaN grown on top was measured and confirmed to be resistive. Any measured conductivity in the other samples hence should arise from mobile carriers at the undoped InGaN/AlN interface. All the samples except sample C and F showed Hall conductivity with a positive Hall coefficient. The results of the Hall-effect measurements are summarized in Table 1. Sample G, the GaN/AlN sample, shows a 300 K 2DHG density of ≈4.5 × 10^{13} cm^{-2} as expected.[4] Among the InGaN/AlN samples, sample C and F are found to be resistive. The polarization-induced 2DHG density is most likely absent in Sample C as the $In_{0.02}Ga_{0.92}N$ thickness of 3.1 nm is very close to the critical thickness d_0 ≈ 3 nm to induce the 2DHG. High resistance in sample F could be due to the high density of mistfit dislocations at the InGaN/AlN interface generated by the relaxation of the InGaN layer. Interestingly, the room temperature 2DHG densities for all conductive InGaN/AlN samples are greater than 1 × 10^{14} cm^{-2}, which is more than 2 × the GaN/AlN 2DHG density! The Hall mobilities range around 0.5–4 cm^2 V^{-1} s^{-1} at room temperature, and increase to 2–10 cm^2 V^{-1} s^{-1} at 77 K. The carriers do not freeze-out at cryogenic temperatures and show repeatable increase in mobilities upon cooling—confirming the presence of high-density 2DHGs in these undoped InGaN/AlN heterostructures. The best measured Hall mobilities and charge densities are 2.6/9.8 cm^2 V^{-1} s^{-1} and 1.47/0.59 × 10^{14} cm^{-2} at 300 K/77 K respectively for sample A with 11 nm $In_{0.07}Ga_{0.93}N$. These represent the first time that such high 2D charge densities are measured in a single channel III-nitride semiconductor system.

Figure 4 compares the experimentally measured 2DHG Hall densities in the InGaN/AlN samples to the expected densities p_s calculated using a self-consistent 1D Schrodinger Poisson solver.[23] The densities are calculated as a function of InGaN thickness for the grown compositions. The simulations assume a temperature of 300 K, however no significant variation in p_s is observed on lowering the temperature to 77 K in the simulation. The GaN/AlN 2DHG density (sample G) agrees with what is expected. A clear discrepancy is observed in the expected and observed InGaN/AlN 2DHG densities. The expected hole densities for the InGaN/AlN with low In composition of 2–9% is expected to have 2DHG densities in the range of ≈6 × 10^{13} cm^{-2}. However we observe high 2DHG densities of >1 × 10^{14} cm^{-2} at room temperatures in all the grown samples, which is 2 × the expected value. The measured 2DHG densities decrease upon cooling for all the samples, including the GaN/AlN 2DHG. This temperature-dependent 2DHG density behavior is similar to previously reported GaN/AlN 2DHGs.[4,24] The Hall densities are however repeatable across Hall-effect measurements and samples grown on different MBE systems. The reason for this discrepancy is not yet understood and needs further investigation.

Sample A with 11 nm $In_{0.07}Ga_{0.93}N$ 2DHG was chosen for further investigation of hole transport in this high-density 2DHG system in comparison to the control sample G. **Figure 5** shows the temperature-dependent Hall-effect measurement results from 300 K down to 10 K on samples A and G. The InGaN/AlN 2DHG density show a 2× increase compared to the GaN/AlN 2DHG density throughout the temperature range down to 10 K, as seen in Figure 5a. This also shows the robustness of the 2DHG with temperature. The InGaN/GaN 2DHG mobility is ≈3 cm^2 V^{-1} s^{-1} at 300 K and increases with cooling, reaching ≈15 cm^2 V^{-1} s^{-1} at 10 K, as seen in Figure 5b. The trend in temperature-dependent mobilities is similar to what is observed in GaN/AlN 2DHGs.[4] The GaN/AlN 2DHGs show mobilites ≈25/190 cm^2 V^{-1} s^{-1} at 300 K/10 K. The InGaN/GaN 2DHG mobilities are considerably lower than GaN/AlN 2DHG mobilities, albeit at a higher charge density. Their high charge density however results in a InGaN/GaN 2DHG sheet resistance of ≈15/10 kΩ per sq. at 300 K/10 K, which is comparable to the GaN/AlN 2DHGs used in state-of-art p-channel FETs.[12,25] Hence, even with the lower room temperature hole mobilities, the InGaN/GaN 2DHG is suitable for device applications as source and drain regions to prevent source starvation.

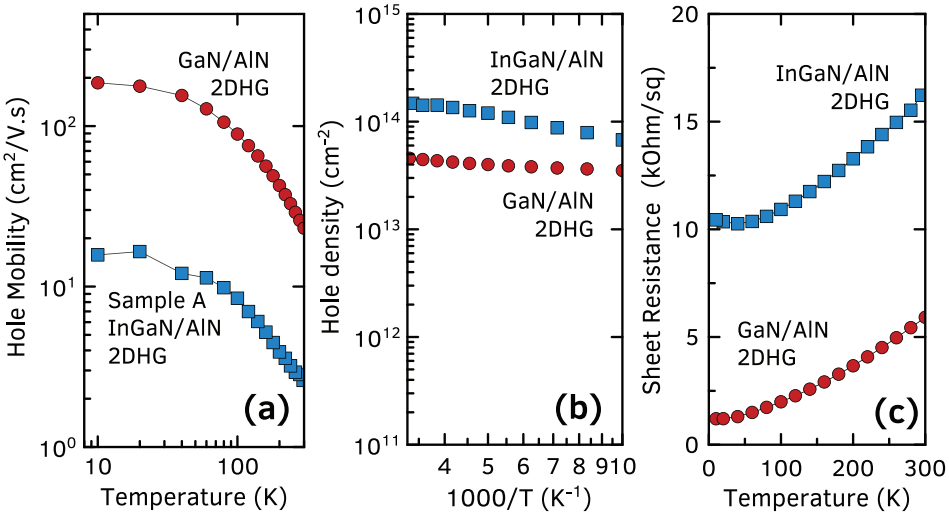

Figure 5. Temperature dependent Hall-effect measurement results for an InGaN/AlN 2DHG (sample A) and a GaN/AlN 2DHG (sample G). a) The InGaN/AlN 2DHG charge density is double that of the GaN/AlN 2DHG throughout the temperature range. b) The 2DHG mobility however is about 10× lower in the InGaN/AlN 2DHG, with a 300 K (10 K) mobility of ≈3 cm^2 V^{-1} s^{-1} (≈18 cm^2 V^{-1} s^{-1}). c) The InGaN/AlN 2DHG room temperature sheet resistance of ≈15 kΩ per sq. is competitive to the other 2DHGs demonstrated in III-nitrides.

How do we increase the room-temperature moblities of these high-density 2DHGs? To answer this, first the limiting carrier scattering mechanism needs to be understood. In GaN/AlN 2DHGs, the room temperature mobilities are limited by acoustic phonon (AP) scattering.[26,27] The acoustic-phonon limited hole mobility μ_{AP} for a 2DHG with density p_s at temperature T under the single parabolic valence band approximation is given by [28]

$$\mu_{AP}(p_s,x) \approx \frac{16e\,\rho\,v_s^2\,\hbar^3}{3k_B T\,D_{ac}^2\,m^*(x)^2\,b(p_s,x)} \tag{2}$$

where where e is the electron charge, ħ is the reduced Planck's constant and k_B is the Boltzmann constant. D_{ac} = 6.2 eV is the acoustic phonon deformation potential.[27] $m^\star(x)$ is effective mass of holes in InGaN of composition x, interpolated between the effective heavy-hole mass of GaN ($2m_0$) and InN (1.6 m_0), where m_0 is the free electron mass. Note that the $m^\star$ for holes in InGaN is lower than that of GaN. $b(p_s, x) = [(33m^\star(x)e^2 p_s)/(8\hbar^2\epsilon_0\epsilon_s)]^{1/3}$ is the variational Fang–Howard wavefunction parameter that quantifies the spatial spread of the 2DHG.

Because of the ≈2 × higher carrier density p_s, acoustic phonon scattering limited mobility μ_{AP} is expected to be lower in the InGaN/AlN 2DHG system compared to GaN/AlN. Additionally, scattering is also expected from mechanisms specific to alloyed crystal channels. In particular, carriers experience scattering from the disorder they see in the crystal potential, that is, alloy disorder scattering. Quantitatively, under a single parabolic valence band approximation, the alloy disorder limited mobility μ_{Alloy} of 2D hole carriers in an alloy channel with composition x is given by [29]

$$\mu_{alloy}(p_s,x) \approx \frac{e\hbar^3}{m^*(x)^2\,\Omega_0(x)^2\,U_{AL}^2\,x(1-x)} \cdot \frac{16}{3\,b(p_s,x)} \tag{3}$$

where $\Omega_0(x) = \sqrt{3}/2 \cdot a_0(x)^2\,c_0(x)$ is the volume of the wurtzite unit cell, where a_0 and c_0 are the interpolated in-plane and out-of-plane lattice constants of InGaN. U_{AL}, the alloy fluctuation potential, is the on-site potential difference if Ga atom is replaced an In atom or vice versa. The value of U_{AL} represents the strength or sensitivity of the alloy scattering, and is typically on the order of the corresponding band offset between the constituents of the alloy. U_{AL} for an alloy is typically extracted by fitting to experimental data. Effect of alloy disorder scattering on electrons has previously been investigated in III-nitride semiconductors, both for 2D electrons in AlGaN[30] and InGaN channels,[31,32] and bulk polarization-doped graded structures.[33] Similar investigations of alloy scattering of holes have not yet been reported. Hole transport has been studied in Mg-doped bulk alloys. In Mg-doped InGaN,[34] a decrease in room temperature hole mobility with increasing In concentration upto x = 0.25 was observed, mobilites remaining below 10 cm^2 V^{-1} s^{-1} throughout. However, the added presence of impurity scattering and the freezing out of holes at low temperatures in Mg-doped InGaN layers do not allow for an in-depth probe of the alloy disorder scattering. The polarization-induced, undoped InGaN/AlN 2DHG therefore offers an unique opportunity to study this scattering mechanism.

Using Equations (2) and (3) , μ_{AP} and μ_{Alloy} for $In_xGa_{1-x}N$/AlN 2DHG at room temperature are calculated as a function of indium content x = 0 to 0.1 for 2DHGs densities of p_s = (0.5, 1, 1.5) × 10^{14} cm^{-2}. GaN physical constants of density ρ = 6.15 × 10^3 kg m^{-3} and sound velocity v_s = 7963 m s^{-1} are used as an approximation for low-composition InGaN with x < 0.1. The total mobility μ_{tot} limited by AP and alloy disorder scattering is then calculated according to Matthiessen's Rule $\mu_{tot}^{-1} = \mu_{Alloy}^{-1} + \mu_{AP}^{-1}$. The results are plotted in **Figure 6**, along with the measured Hall data of InGaN/AlN 2DHGs from Table 1. Note that the Hall factor is unity because of the heavily degenerate 2DHG density.

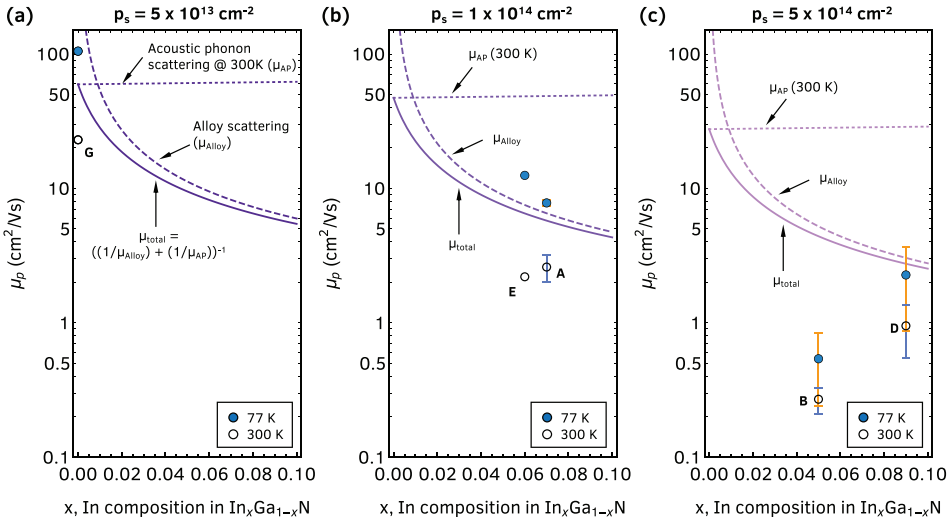

Figure 6. The experimental and theoretical room-temperature total hole mobility as a function of the InGaN composition. The model considers scattering due to acoustic phonons (AP) and alloy disorder, for different 2DHG densities p_s a) 5×10^{13} cm^{-2}, b) 1×10^{14} cm^{-2}, and c) 5×10^{14} cm^{-2}. Unlike the case of GaN/AlN 2DHGs,[25] alloy disorder scattering is expected to dominate in InGaN/AlN 2DHGs, limiting the hole mobilities to below the intrinsic phonon limit at room temperature. The experimental data measured in this work concurs with the theoretical predictions for an alloy disorder potential $U_{AL} \approx 1$ eV.

A reasonable agreement is observed between the calculated hole mobilities with $U_{AL} = 1.0$ eV and the experimentally measured Hall mobilities. It is observed that AP scattering does not change significantly within the indium concentration range of $x = 0$ to 0.1. The alloy disorder limited scattering is observed to be the dominant scattering mechanism for 2DHGs in InGaN/AlN with In composition $x > 0.01$. μ_{alloy} is a strong function of x, and decreases down from ≈50 cm^2 V^{-1} s^{-1} at $x = 0.01$ to ≈6 cm^2 V^{-1} s^{-1} at $x = 0.1$ for $p_s = 5 \times 10^{13}$ cm^{-2}. The observed deviation from the calculated value in sample B is attributed to the InGaN layer being very thin (4 nm) and therefore the 2DHG being very close to other possible remote scattering centers on the surface.[35] The alloy fluctuation potential $U_{AL} = 1.0$ eV for holes in InGaN agrees with reported the valence band offset[36] between InN and GaN $\Delta E_v \approx 1.07$ eV. Interestingly, this potential is lower than the $U_{AL} \approx 1.68$ eV for electrons in InGaN.[32] This is physically expected since the effect of Ga by In cation substitution has a lower effect on the p-orbital like valence bands which primarily from the N atoms, than the s-orbital like conduction bands. If $\Omega_0(x)$ is considered to be the effective volume Ga or In cation occupies in the unit cell as $\Omega_0(x) = \sqrt{3}/8 \cdot a_0(x)^2 \, c_0(x)$, then $U_{AL} = 1.9$ eV results in the best fit to the experimental data.

It is clear from the calculated model and supporting experimental data that, unlike the case in Si/SiGe,[37] the effect of alloy scattering in these InGaN/AlN 2DHGs dominate over the effect of decreasing hole effective mass in the alloy. Hence, a path to higher 2DHG mobility through alloying might not be feasible. However carefully engineered in-plane strain [26,38] could potentially be used to boost the mobility of these InGaN/AlN and decrease their sheet resistances further. Application of uniaxial, in-plane 1) compressive strain in the direction of hole transport, or 2) tensile strain applied perpendicular to the hole transport have been predicted[26] to reduce the valence band hole effective mass m^*, which should translate to a higher alloy scattering limited hole mobility through Equation (3).

4. Conclusions

To summarize, this work reports of the observation of very high 2D hole densities of $>1 \times 10^{14}$ cm^{-2} in thin, pseudomorphic, low-In-composition InGaN layers on AlN. It is observed that introducing indium in the GaN channel layer of a GaN/AlN 2DHG boosts the 2DHG densities. The high in-plane lattice mismatch between InGaN and AlN leads to a high piezoelectric polarization component which in turn boosts the 2DHG densities. The theoretical critical thickness of pseudomorphic InGaN layers on AlN is calculated using Fischer's strain-relaxation model, and is used as a guide to design and grow these pseudomorphic layers using MBE. Temperature dependent Hall-effect measurements confirm the high densities of 2DHG in these layers. The hole densities measured in this work are the highest charge densities measured at a single III-nitride interface. **Figure 7** shows a benchmark plot comparing InGaN/GaN 2DHGs to other semiconductor 2D hole systems. InGaN/GaN 2DHGs have among the highest densities across all material systems, and just an order lower than the 2D crystal limit of ≈10^{15} cm^{-2}. The large density of holes provide an epitaxial platform for investigation of scientific phenomena by possible integration of other compatible materials[24] such as ferrimagnetic Mn_4N. AlGaN/AlN heterostructures designed using similar principles as presented here could be used for applications which need $p_s < 5 \times 10^{13}$ cm^{-2}.

The room temperature sheet resistances of these InGaN/AlN 2DHGs are ≈15 kΩ per sq., which make them candidates for enabling low-resistance p-type regrown contacts to the GaN/AlN 2DHG for device applications. As-grown p++InGaN

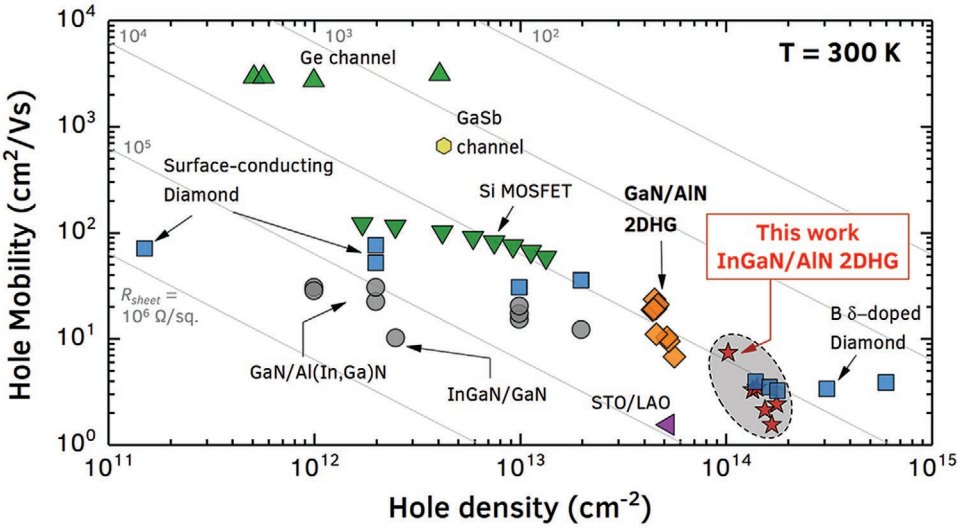

Figure 7. Benchmark plot comparing the 2DHGs in this work with the previously reported 2DHGs in III-nitride semiconductor heterostructures, and other material systems. The InGaN/GaN 2DHGs are amongst the highest density hole channels reported across material systems including Ge channels, GaSb channels, Si p-MOSFET channels, diamond, and oxides.

contact layers to the GaN/AlN 2DHG channel have enabled the lowest p-type contact resistivities[25] in GaN/AlN pFETs.[12] However, the presence of these p-doped contact layers require complicated fabrication process to monolithically integrate the GaN/AlN pFET with its n-type analog, the AlN/GaN/AlN HEMTs.[39] The demonstration of the InGaN/AlN 2DHG opens up the possibility of a better alternative in the form of selective-area regrown InGaN contacts. In a GaN/AlN heterostructure, the GaN layer is etched away selectively in photolithographically-defined ohmic/access regions and InGaN is regrown in those regions. This should yield high-density InGaN/AlN 2DHGs in the ohmic/access regions which makes a 2D–2D valence band contact to the GaN/AlN 2DHG under the gate. This should lower the p-type contact resistances in these pFETs even further, while maintaining integration possibilities for wide-bandgap CMOS.[11,40] Additionally, the in-plane strain in these regrown InGaN regions can be engineered to test the effect on 2DHG mobility.[26]

The survival of the InGaN/AlN 2DHGs at cryogenic temperatures offers a unique platform of studying alloy disorder effects on the hole transport when phonons are frozen out. This study presents the first such investigation of the alloy disorder scattering of holes in III-nitride semiconductors. It is found that the room temperature mobilities in these 2DHGs are limited by alloy disorder scattering as opposed to acoustic phonon scattering. A characteristic alloy-disorder potential of 1.0 eV is extracted for holes in InGaN. This results in room-temperature 2D hole mobilities in InGaN to be lower than in GaN, albeit at higher charge densities. This is contrary to observations[37] in narrow bandgap semiconductor channels such as SiGe, where the phonon scattering dominates over the alloy scattering at room temperature, and therefore alloying leads to higher mobility holes compared to Si due to lower hole effective mass.

These InGaN/AlN 2DHGs have been grown on different wafers and MBE systems and are found to be robust and repeatable. Even though these 2DHG densities are expected to be higher than those of GaN/AlN 2DHGs, quantitatively the densities are much higher than predicted. These values cannot be explained by the accepted polarization theory[1,13] or the recently proposed corrected polarization constants[41] for III-nitride semiconductors. The origin of these large hole densities is therefore presented as an open question which requires further investigation. A controlled study of transport in InGaN/AlN samples with series of InGaN thickness by keeping the composition constant, or vice versa should yield valuable insights and help provide the answers. Tracking the strain in higher In composition InGaN layers should also help provide insights into the strain evolution in these InGaN/AlN heterostructures better. Although Fischer model can explain the trend in the experimental data in Figure 2b, more experimental points at higher compositions will allow for better comparison to other critical thickness models.[42] The recent advancements[5,18,43] in homoepitaxial growths of AlN provide an ideal platform for such studies in structurally and chemically pure heterostructures.

5. Experimental Section

Molecular Beam Epitaxy of InGaN/AlN Heterostructures: InGaN on AlN heterostructures studied in this work were grown using plasma assisted molecular beam epitaxy (PA-MBE) on metal-polar MOCVD-grown AlN on sapphire templates. Diced 8 mm × 8 mm substrates pieces were ultrasonicated in acetone/methanol/propanol for 10 min each, and then mounted on lapped Si wafers using molten indium. The substrates were outgassed at 200 °C for 7 h and 500 °C for 2 h before introducing into the growth chamber with idle pressure of 10^{-10} Torr. The growth rate of 0.42 µm h^{-1} was controlled by the N-plasma RF power of 400 W. A ≈400 nm thick AlN buffer layer was grown at T_{sub} = 790 °C in metal-rich conditions.[44] Impurity blocking layers (IBLs) were incorporated into the AlN buffer layer[27] to minimize the effect of impurities from the substrate on the 2DHG transport and compensation. After the growth of AlN buffer layer, the substrate was cooled down to T_{sub} = 655 °C for the growth of the InGaN layer during an ≈2.5 min growth interruption. Different InGaN layer thicknesses and compositions were obtained varying the Ga (Φ_{Ga}) and In (Φ_{In}) fluxes with respect to active N flux (Φ_N) and shutter open times. The relative flux conditions

of $\Phi_{Ga} + \Phi_{In} > \Phi_N$, $\Phi_{Ga} < \Phi_N$ were maintained to ensure N-limited InGaN MBE growth conditions.[45,46] All the layers were unintentionally-doped. The surface crystal structures were monitored using an in situ reflection high-energy electron diffraction setup, which remained streaky throughout the growth. After unloading from the MBE system, all the samples were dipped in concentrated HCl solution for ≈15 min to remove any excess metal droplets of Ga or In present on the surface before any further characterization.

Hall-effect Measurements of the 2DHG: The Hall-effect measurements performed in this work were performed on unprocessed, 8 mm × 8 mm sample pieces. Ohmic contacts to the 2DHG buried in the InGaN layer were made using soldered Indium dots, ⩽1 mm^2 in size, at the four corners of the sample in a Van der Pauw configuration. The Hall-effect measurements at 300 and 77 K were performed using a nanometric Hall-effect system HL5500, using a 0.32 T magnetic field provided by a permanent magnet. Liquid nitrogen was used to immerse the sample for the obtaining the data at 77 K.

The temperature dependent Hall-effect measurements were performed in a Lakeshore Cryogenics Hall-effect measurement system at magnetic field of 1 T. The temperature was varied from 300 to 10 K using a closed-cycle cryogenic stage.

Acknowledgements

This work was supported by AFOSR (grant FA9550-20-1-0148) and NSF (grants 1710298, 1534303). Characterizations and measurements were carried out in part at CNF, supported by NSF Grant NNCI-2025233, and in part at CCMR Shared Facilities, supported through the NSF MRSEC program (DMR-1719875) and NSF MRI (DMR-1429155 and DMR-1338010) programs.

Conflict of Interest

The authors declare no conflict of interest.

Data Availability Statement

The data that support the findings of this study are available from the corresponding author upon reasonable request.

Keywords

2D hole gas, molecular beam epitaxy, heterostructures

Received: October 14, 2021
Revised: November 23, 2021
Published online:

[1] O. Ambacher, J. Smart, J. R. Shealy, N. G. Weimann, K. Chu, M. Murphy, W. J. Schaff, L. F. Eastman, R. Dimitrov, L. Wittmer, M. Stutzmann, W. Rieger, J. Hilsenbeck, *J. Appl. Phys.* **1999**, *85*, 3222.
[2] Y. J. Cho, Y. Ren, H. G. Xing, D. Jena, *Appl. Phys. Express* **2019**, *12*, 121003.
[3] R. Chaudhuri, A. Hickman, J. Singhal, J. Casamento, H. G. Xing, D. Jena, *Phys. Status Solidi A* **2021**.
[4] R. Chaudhuri, S. J. Bader, Z. Chen, D. A. Muller, Huili, Xing, D. Jena, *Science* **2019**, *365*, 1454.
[5] Z. Zhang, J. Encomendero, R. Chaudhuri, Y. Cho, V. Protasenko, K. Nomoto, K. Lee, M. Toita, H. G. Xing, D. Jena, *Appl. Phys. Lett.* **2021**, *119*, 162104.
[6] P. Kozodoy, H. Xing, S. P. DenBaars, U. K. Mishra, A. Saxler, R. Perrin, S. Elhamri, W. C. Mitchel, *J. Appl. Phys.* **2000**, *87*, 1832.
[7] A. Nakajima, Y. Sumida, M. H. Dhyani, H. Kawai, E. M. S. Narayanan, *Appl. Phys. Express* **2010**, *3*, 12.
[8] G. Li, R. Wang, B. Song, J. Verma, Y. Cao, S. Ganguly, A. Verma, J. Guo, H. G. Xing, D. Jena, *IEEE Electron. Device Lett.* **2013**, *34*, 852.
[9] H. Hahn, B. Reuters, A. Pooth, B. Hollander, M. Heuken, H. Kalisch, A. Vescan, *IEEE Trans. Electron Devices* **2013**, *60*, 3005.
[10] K. Zhang, M. Sumiya, M. Liao, Y. Koide, L. Sang, *Sci. Rep.* **2016**, *6*, 23683.
[11] S. J. Bader, H. Lee, R. Chaudhuri, S. Huang, A. Hickman, A. Molnar, H. G. Xing, D. Jena, H. W. Then, N. Chowdhury, T. Palacios, *IEEE Trans. Electron. Devices* **2020**, *67*, 4010.
[12] K. Nomoto, R. Chaudhuri, S. J. Bader, L. Li, A. Hickman, S. Huang, H. Lee, T. Maeda, H. W. Then, M. Radosavljevic, P. Fischer, A. Molnar, J. C. M. Hwang, H. G. Xing, D. Jena, *2020 IEEE International Electron Devices Meeting, IEDM*, IEEE, Piscataway, NJ **2020**, pp. 8.3.1–8.3.4.
[13] F. Bernardini, V. Fiorentini, D. Vanderbilt, *Phys. Rev. B: Condens. Matter Mater. Phys.* **1997**, *56*, R10024.
[14] T. Takeuchi, H. Takeuchi, S. Sota, H. Sakai, H. Amano, I. Akasaki, *Jpn. J. Appl. Phys., Part 2: Lett.* **1997**, *36*, 2 SUPPL. B L177.
[15] M. Leyer, J. Stellmach, C. Meissner, M. Pristovsek, M. Kneissl, *J. Cryst. Growth* **2008**, *310*, 4913.
[16] A. Fischer, H. Kiihne, H. Richter, *Phys. Rev. Lett.* **1994**, *73*, 2712.
[17] G. Koblmueller, R. Averbeck, L. Geelhaar, H. Riechert, W. Hösler, P. Pongratz, *J. Appl. Phys.* **2003**, *93*, 9591.
[18] K. Lee, Y. Cho, L. J. Schowalter, M. Toita, H. G. Xing, D. Jena, *Appl. Phys. Lett.* **2020**, *116*, 26.
[19] J. W. Matthews, A. E. Blakeslee, *J. Cryst. Growth* **1974**, *27*, 118.
[20] Y. Cao, Ph.D. Thesis, University of Notre Dame, Notre Dame **2010**.
[21] B. Heying, E. J. Tarsa, C. R. Elsass, P. Fini, S. P. DenBaars, J. S. Speck, *J. Appl. Phys.* **1999**, *85*, 6470.
[22] B. Liu, R. Zhang, J. G. Zheng, X. L. Ji, D. Y. Fu, Z. L. Xie, D. J. Chen, P. Chen, R. L. Jiang, Y. D. Zheng, *Appl. Phys. Lett.* **2011**, *98*, 10.
[23] S. Birner, T. Zibold, T. Andlauer, T. Kubis, M. Sabathil, A. Trellakis, P. Vogl, *IEEE Trans. Electron Devices* **2007**, *54*, 2137.
[24] Z. Zhang, Y. Cho, M. Gong, S. T. Ho, J. Singhal, J. Encomendero, X. Li, H. Lee, H. G. Xing, D. Jena, *IEEE Trans. Magn.* **2021**, https://doi.org/10.1109/TMAG.2021.3085853.
[25] S. J. Bader, R. Chaudhuri, A. Hickman, K. Nomoto, S. Bharadwaj, H. W. Then, H. G. Xing, D. Jena, *2019 IEEE International Electron Devices Meeting, IEDM*, IEEE, Piscataway, NJ **2019**, pp. 4.5.1–4.5.4.
[26] S. J. Bader, R. Chaudhuri, M. F. Schubert, H. W. Then, H. G. Xing, D. Jena, *Appl. Phys. Lett.* **2019**, *114*, 25.
[27] R. Chaudhuri, Z. Chen, D. A. Muller, H. G. Xing, D. Jena, *J. Appl. Phys.* **2021**, *130*, 025703.
[28] J. H. Davies, *The Physics of Low-Dimensional Semiconductors*, Cambridge University Press, Cambridge **1997**.
[29] G. Bastard, *Wave Mechanics Applied to Semiconductor Heterostructures*, Wiley-Interscience, Hoboken, NJ **1988**.
[30] M. Miyoshi, S. Fujita, T. Egawa, *Appl. Phys. Express* **2015**, *8*, 051003.
[31] P. Sohi, J. F. Carlin, N. Grandjean, *Appl. Phys. Lett.* **2018**, *112*, 26.
[32] V. K. Singh, D. N. Nath, *Phys. Status Solidi A* **2018**, *215*, 1700757.
[33] J. Simon, A. Wang, H. Xing, S. Rajan, D. Jena, *Appl. Phys. Lett.* **2006**, *88*, 042109.
[34] S. J. Chang, C. H. Chen, P. C. Chang, Y. K. Su, P. C. Chen, Y. D. Jhou, H. Hung, S. M. Wang, B. R. Huang, *IEEE Trans. Electron Devices* **2003**, *50*, 2567.
[35] Y. Cao, H. Xing, D. Jena, *Appl. Phys. Lett* **2010**, *97*, 222116.

[36] K. Wang, C. Lian, N. Su, D. Jena, J. Timler, *Appl. Phys. Lett.* **2007**, *91*, 232117.
[37] M. J. J. Kearney, A. I. I. Horrell, *Semicond. Sci. Technol.* **1998**, *13*, 174.
[38] C. Gupta, Y. Tsukada, B. Romanczyk, S. S. Pasayat, D. A. James, E. Ahmadi, S. Keller, U. K. Mishra, *Jpn. J. Appl. Phys.* **2019**, *58*, 030908.
[39] A. Hickman, R. Chaudhuri, L. Li, K. Nomoto, S. J. Bader, J. C. Hwang, H. G. Xing, D. Jena, *IEEE J. Electron Devices Soc.* **2020**, *9*, 121.
[40] A. L. Hickman, R. Chaudhuri, S. J. Bader, K. Nomoto, L. Li, J. Hwang, H. G. Xing, D. Jena, *Semicond. Sci. Technol.* **2021**, *36*, 044001.
[41] C. E. Dreyer, A. Janotti, C. G. Van de Walle, D. Vanderbilt, *Phys. Rev. X* **2016**, *6*, 021038.
[42] D. Holec, P. M. Costa, M. J. Kappers, C. J. Humphreys, *J. Cryst. Growth* **2007**, *303*, 314.
[43] Y. Cho, C. S. Chang, K. Lee, M. Gong, K. Nomoto, M. Toita, L. J. Schowalter, D. A. Muller, D. Jena, H. G. Xing, *Appl. Phys. Lett.* **2020**, *116*, 172106.
[44] R. Chaudhuri, S. J. Bader, Z. Chen, D. Muller, H. G. Xing, D. Jena, *Phys. Status Solidi (B)* **2020**, *257*, 1900567.
[45] C. Adelmann, R. Langer, G. Feuillet, B. Daudin, *Appl. Phys. Lett.* **1999**, *75*, 3518.
[46] T. Böttcher, S. Einfeldt, V. Kirchner, S. Figge, H. Heinke, D. Hommel, H. Selke, P. L. Ryder, *Appl. Phys. Lett.* **1998**, *3232*, 20.